JOURNAL OF AIRCRAFT
Vol. 33, No. 1, January–February 1996

Helicopter Rotor Blade Computation in Unsteady Flows Using Moving Overset Grids

Jasim Ahmad*
Sterling Software, Moffett Field, California 94035-1000
and
Earl P. N. Duque†
U.S. Army Aeroflightdynamics Directorate, Moffett Field, California 94035-1000

An overset grid thin-layer Navier–Stokes code has been extended to include dynamic motion of helicopter rotor blades through relative grid motion. The unsteady flowfield and airloads on an AH-IG rotor in forward flight were computed to verify the methodology and to demonstrate the method's potential usefulness towards comprehensive helicopter codes. In addition, the method uses the blade's first harmonics measured in the flight test to prescribe the blade motion. The solution was impulsively started and became periodic in less than three rotor revolutions. Detailed unsteady numerical flow visualization techniques were applied to the entire unsteady data set of five rotor revolutions and exhibited flowfield features such as blade vortex interaction and wake roll-up. The unsteady blade loads and surface pressures compare well against those from flight measurements. Details of the method, a discussion of the resulting predicted flowfield, and requirements for future work are presented. Overall, given the proper blade dynamics, this method can compute the unsteady flowfield of a general helicopter rotor in forward flight.

Introduction

THE accurate computation of a helicopter flowfield is essential for proper and efficient airload predictions in forward flight and hover. The constantly changing aerodynamic environment and loads are important features of rotorcraft aerodynamics. Strong tip vortices in the rotor wakes dominate the flowfield to produce a highly unsteady and nonuniform induced velocity field at the rotor disk. Recent emphasis on numerical simulation procedures for complex flows have made it possible to accurately obtain rotor blade aerodynamic characteristics by solving the governing differential equations.

Descriptions of various computational fluid dynamics (CFD) methods for rotorcraft problems based on the solution of full-potential, Euler, and Navier–Stokes equations can be found in the literature. Notable among them is the introduction of embedded or overset grid scheme to the existing single grid scheme by Duque and Srinivasan.[1] Also, Srinivasan et al.[2,3] used a thin-layer Navier–Stokes method for forward-flight simulation of a nonlifting rotor blade as well as rotor in hover. Chen et al.[4] and Agarwal and Deese[5] solved the Euler equations.

Unlike fixed wing aircraft, the helicopter airloads depend greatly upon the unsteady dynamic motion of the blades. To model the blade motion, comprehensive helicopter analysis methods have been developed that use aerodynamic and wake models coupled to structural dynamic models. The aerodynamics are typically based upon lifting-line theory and depend upon either linear methods or two-dimensional experimental airfoil data with corrections for unsteady and three-dimensional effects.

Notable among the comprehensive helicopter analysis codes is CAMRAD/JA by Johnson.[6] To account for compressibility, three-dimensional effects, and arbitrary blade geometries, Strawn and Tung[7] coupled CAMRAD to the full potential rotor (FPR) code. Strawn et al.[8] demonstrated the capability to model rotors in forward flight using the coupled CAMRAD and FPR by computing the airloads of the Puma rotor.

Hernandez and Johnson[9] used the coupled CAMRAD/JA-FPR method to compute the AH-1G rotor in forward flight. They were able to compare well against flight test data. In addition, they found that tip core size specifications have a large effect upon the predicted rotor loads.

Ramachandran et al.[10] developed a method based upon the vorticity-embedding technique. This method solves the unsteady full potential equation on a Eulerian grid with an overset Lagrangian vortical velocity field. He also applied his method to the forward flight of the AH-1G rotor system with favorable comparisons to flight tests.

All of the above methods use single-structured grids. Single grids have limited use. For example, it would be very difficult to use a single-structured grid to investigate the aerodynamic interference between either a rotor and fuselage or the aerodynamic interference between a rotor and the rotor hub. In addition, almost all of the above methods use wake models to include the influence of the wake. Wake models limit the method's generality and require considerable adjustments to their approximations to obtain accurate solutions.

The work summarized herein uses an alternative griding method known as overset grids or the Chimera method[11] to allow for blade motions and to accurately compute the vortical wake from first principles. The overset-grid scheme greatly simplifies arbitrary blade motions, which is important in achieving trimmed flight conditions, as well as in predicting airloads accurately in an effort to develop a comprehensive helicopter analysis method. Also, with overset grids one can more easily discretize the domain with simple well-defined grids that accurately compute the rotor wake.

Until recently, few methods were able to solve the transient flow about multiple bodies moving relative to one another. Meakin[12] computed the unsteady flowfield of the V-22 tiltrotor aircraft, including the rotor rotation, by solving the un-

Presented as Paper 94-1922 at the AIAA 12th Applied Aerodynamics Conference, Colorado Springs, CO, June 20–22, 1994; received Sept. 23, 1994; revision received May 10, 1995; accepted for publication June 24, 1995.

*Research Scientist, NASA Ames Research Center, MS 258-1. Member AIAA.

†Research Scientist, NASA Ames Research Center, Aviation and Troop Command. Member AIAA.

steady thin-layer Navier–Stokes equations on moving overset grids. To accomplish this calculation, he developed a method that determines the interpolation coefficients between the overset grids. His domain connectivity algorithm (DCF) was verified in detail in his work. But the set of flight conditions he considered were hypothetical and did not include the dynamic pitch, flap, or lag motions of the rotor blades. The method presented here accounts for the blade motion by appropriately moving the overset grid system according to the blade harmonics measured in a flight test.

In summary, a numerical method that computes the unsteady flowfield of a helicopter rotor in forward-flight or hover is presented. The method solves the thin-layer Navier–Stokes equations on a system of moving overset grids and uses the blade harmonics measured in flight to prescribe the blade motions. Comparisons between computed and flight-test unsteady blade loads and surface pressures of the AH-1G helicopter are presented. Numerical flow visualizations exhibit flowfield features such as blade-vortex interaction and wake roll-up. This article provides details of the method, a discussion of the resulting predicted flowfield, and demonstrates the capability to model the unsteady flowfield of an arbitrary helicopter rotor in forward flight.

Methodology

Algorithm

The single-grid flow solver developed by Srinivasan et al.[2] with overset-grid modifications implemented by Duque and Srinivasan[1] was employed in the study. Calculations by Srinivasan and Ahmad[13] have demonstrated the method's versatility by computing the hovering flowfield of a rotor and whirl stand. The method solves the thin-layer Navier–Stokes equations shown in Eq. (1):

$$\frac{\partial}{\partial t}\hat{Q} + \frac{\partial}{\partial \xi}\hat{E} + \frac{\partial}{\partial \eta}\hat{F} + \frac{\partial}{\partial \zeta}\hat{G} = Re^{-1}\frac{\partial}{\partial \zeta}\hat{S} \tag{1}$$

where $\hat{Q} = J^{-1}(\rho, \rho u, \rho v, \rho w, e)$ is the vector of the conserved variables, density, momentum, and energy, scaled by the transformation Jacobian, and $\hat{E}$, $\hat{F}$, $\hat{G}$, and $\hat{S}$ are the scaled inviscid and viscous flux vectors.

With overset grids a sequence of grids are placed such that they lie arbitrarily within a primary grid. For example, Fig. 1 provides an example where an airfoil curvilinear grid lies within a background Cartesian grid. The airfoil grid captures features such as the boundary layers, tip vortices, and shocks, etc. The background grid surrounds the airfoil grid and carries the solution to the far field. The background grid was generated with some knowledge of the airfoil's surface and outer boundary locations. Consequently, some of the background grid points lie within the airfoil's solid body regions and must be removed from the solution. Once removed, hole regions remain within the interior of the larger background grid and create a set of boundary points known as hole-fringe points. The airfoil grid interpolates data to the background grid at the background's hole-fringe points. Conversely, the background grid interpolates data to the airfoil grid at the airfoil outer boundary points.

Within each separate overset grid, different flow solver methods may be used to solve the governing equations of motion. The current method uses an implicit upwind method for all of the individual grids. The method advances the solution in time using the lower–upper symmetric Gauss–Siedel (LU–SGS) implicit scheme by Yoon and Jameson[14] shown in Eqs. (2). The scheme is third-order accurate in space and first-order accurate in time:

$$LD^{-1}U\Delta Q = -IB\Delta t\mathcal{R} \xrightarrow{\text{Solving}} \begin{aligned} Q^* &= -IB\Delta t L^{-1}\mathcal{R} \\ Q^{**} &= DQ^* \\ \Delta Q &= U^{-1}Q^{**} \end{aligned} \tag{2}$$

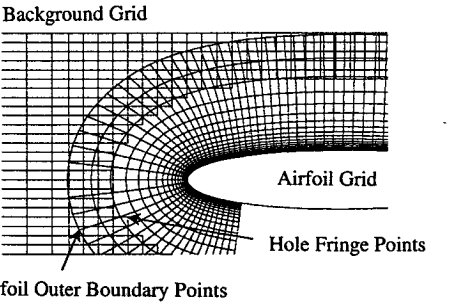

Fig. 1 Schematic of overset grid system.

The matrices L and U are formed by performing either backward or forward differences on the appropriate flux Jacobians A, B, or C as shown in Eqs. (3). In Eqs. (3), Δt is the time step, Δ_ξ and ∇_ξ represent forward and backward differences, respectively, I is the identity matrix, and σ is the spectral radius. The matrix D is a diagonal matrix that completes the back-solve process. This decomposition scheme reduces the required floating point operations in comparison to block tridiagonal methods:

$$\begin{aligned} L &= I + IB_{j,k,l}\Delta t(-A^-_{j,k,l} + \nabla_\xi A^+_n - B^-_{j,k,l} + \nabla_\eta B^+_n \\ &\quad - C^-_{j,k,l} + \nabla_\zeta C^+_n) \\ D &= I + IB_{j,k,l}\Delta t(A^-_n + B^-_n + C^-_n + A^+_n \\ &\quad + B^+_n + C^+_n)_{j,k,l} \\ U &= I + IB_{j,k,l}\Delta t(A^+_{j,k,l} + \Delta_\xi A^-_n + B^+_{j,k,l} \\ &\quad + \Delta_\eta B^-_n + C^+_{j,k,l} + \Delta_\zeta C^-_n) \end{aligned} \tag{3}$$

where $A^\pm = A \pm \sigma_x$.

With overset grids, the additional array IB marks the hole regions within the grid interior by taking on the value of 0. Outside of the hole and in the valid regions of the flowfield the IB array equals 1. The IB array removes the hole regions from the solution set as shown in Eqs. (2).

The flux terms use a Roe upwind-biased scheme for all three coordinate directions with higher-order MUSCL-type limiting to model the shocks accurately.[15] The resulting flux differences are shown in Eq. (4):

$$\mathcal{R} = \nabla_\xi E^+_n + \Delta_\xi E^-_n + \nabla_\eta F^+_n + \Delta_\eta F^-_n + \nabla_\zeta G^+_n + \Delta_\zeta G^-_n \tag{4}$$

At the hole fringe points the flux evaluations reduce to second order at the resulting interior boundaries by modifying the primitive variable evaluations with the IB array. Equation (5) shows the ζ-coordinate flux evaluations:

$$\hat{E}(Q_L, Q_R) \approx \tfrac{1}{2}[\hat{E}(Q_R) + \hat{E}(Q_L) - |A(Q_L, Q_R)|(Q_R - Q_L)] \tag{5}$$

The primitive variable quantities Q are obtained by first-order extrapolation functions at boundaries or third order away from boundaries. As shown in Eqs. (6), these quantities drop to first order through the use of the IB array:

$$\begin{aligned} Q_L &= Q_j + [\tfrac{1}{6}(Q_j - Q_{j-1}) + \tfrac{1}{3}(Q_{j+1} - Q_j)]IB_{j+1}IB_{j-1} \\ Q_R &= Q_{j+1} - [\tfrac{1}{3}(Q_{j+1} - Q_j) + \tfrac{1}{6}(Q_{j+2} - Q_{j+1})]IB_{j-1}IB_{j+1} \end{aligned} \tag{6}$$

Finally, the flow solver assumes fully turbulent flow for the blades and inviscid flow in background grids. The simple algebraic turbulence model of Baldwin and Lomax[16] is used to estimate the eddy viscosity.

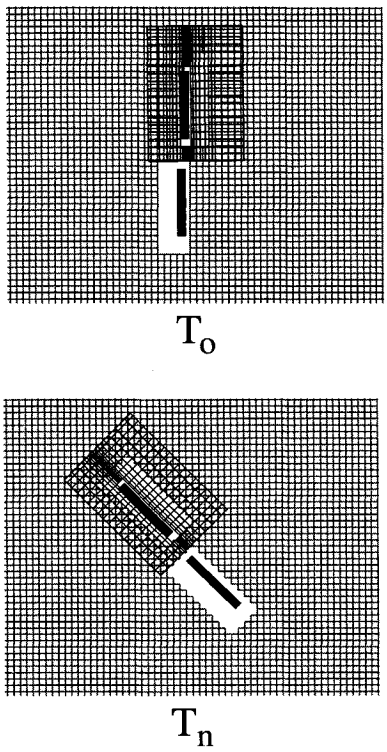

Fig. 2 Moving overset grid schematic.

In overset grids, the quality of the solution interpolation at the boundaries depends on the relative grid cell ARs, skewness, and clustering, etc. It also depends on the boundary's proximity to high flow gradient regions. While forming the grids, one must ensure that the boundaries have adequate overlap, nearly equal cell ARs, and low skewness. Boundaries should also avoid high flow gradients.

With moving overset grids, individual grids move with their appropriate grid motion. As the grids move, the holes and hole boundaries change with time. Figure 2 provides a schematic for a helicopter blade in rotation, with one blade grid omitted for clarity. As the blades rotate from some time state T_0 to another time T_n, the grid attached to the blades rotate along with them. Subsequently, the holes change with the blade rotation as shown.

To determine the grid's changing connectivity and hole points, the code known as domain connectivity functions in three dimensions (DCF3D) by Meakin[12] was employed. DCF3D uses inverse mapping of the computational space to limit the search time and to compute hole and outer-boundary interpolation stencils. The major expense in DCF3D is the creation of the inverse maps. However, the maps are independent of the relative orientation of the grids and so it repeatedly uses the maps during the grid movement.

During the flowfield solution process, intergrid boundaries are constantly created due to the grid movement. After each flow solution time step, grid connectivity data has to be determined. Currently, the flow solver (Chi-TURNS) and the connectivity algorithm (DCF3D) are separate Fortran codes. A UNIX C-Shell script is used to join the two methods.

With each time step, DCF3D obtains the latest connectivity data and hole points. Relevant intergrid boundary data are written to disk. The hole-fringe points are then checked to ensure that they are introduced to the solution gradually. The flow solver then begins the solution process by reading in the DCF3D files from disk, solving the equations of motion, and then moving the grids to the next time step. Once complete, the solution and grids are written to disk and the whole process continues until the desired number of time steps have been completed.

Blade Motion

The method assumes rigid blade motions in flap and pitch. The periodic blade motion for pitch and flap as a function of blade azimuth can be described by a Fourier series[10,17] as shown in Eqs. (7) and (8):

Pitch

$$\theta = \theta_0 + \theta_{1c}\cos\psi + \theta_{1s}\sin\psi + \theta_{2c}\cos 2\psi + \theta_{2s}\sin 2s + \cdots \quad (7)$$

Flap

$$\beta = \beta_0 + \beta_{1c}\cos\psi + \beta_{1s}\sin\psi + \beta_{2c}\cos 2\psi + \beta_{2s}\sin 2s + \cdots \quad (8)$$

Using only the mean and first blade harmonics, Eulerian angles prescribe the blade motion to the flow solver. Euler parameters or Eulerian angles[18] are useful and convenient ways to express motion of rotating bodies in terms of the fixed inertial frame.

In this method, the blade rotates about its spin axis at some given rotational rate. At each time step, the blade rotates through by an increment of ψ that results in a change in pitch and flap. The incremental change in the blade position is then imposed by transforming the position vector through successive matrix multiplications as shown in Eq. (9):

$$T = [A][B][C] \qquad \vec{x}_{\text{new}} = T\vec{x}_{\text{old}} \quad (9)$$

The transformation matrix T consists of the rotation matrices A, B, and C. The matrices A, B, and C represent the various coordinate rotations. See Amirouche[18] for details of the transformation matrices.

Grid System

The grid system consists of five overset grids; one for each rotor blade and one intermediate transition grid for each blade to help connect them to the single global background grid. The rotor grid is of C-H topology with clustering near the tip, root, and leading and trailing edges. Beyond the tip and inboard of the root chord the surface grid collapses to a slit and forms a singular plane that extends approximately one chord length beyond either side. Each rotor blade grid has 119 total chordwise points and 45 points in the spanwise direction that lie on the body. In the normal direction, the first grid point is 0.00003 chords off the body and extends approximately 0.75 chord from the surface in all directions. The hyperbolic grid generator by Chan et al.[19] generated the resulting volume grid illustrated in Fig. 3.

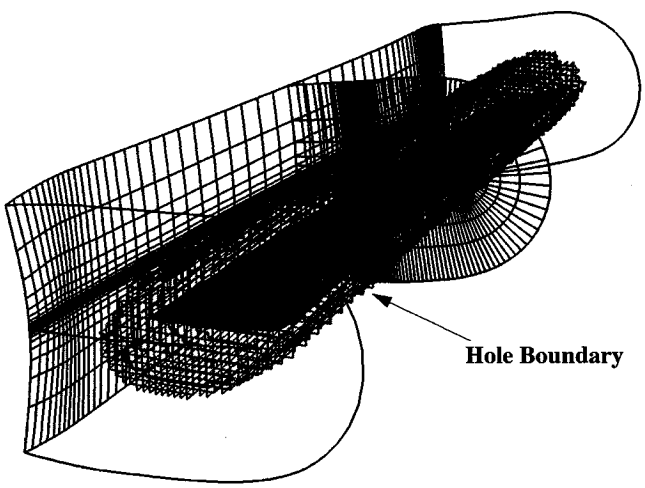

Fig. 3 Blade grid cutting through intermediate grid.

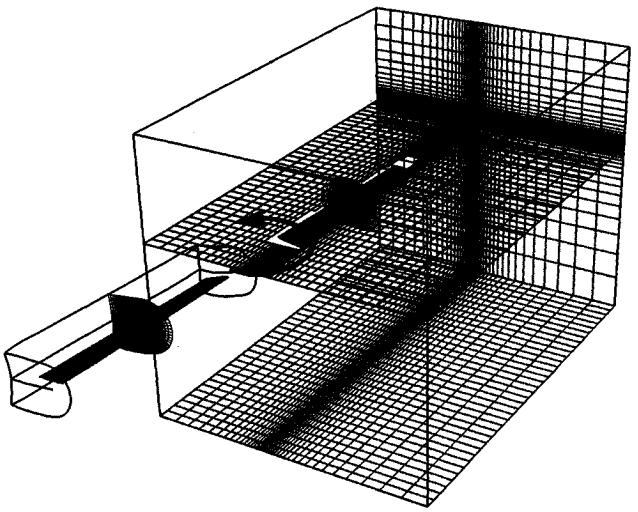

Fig. 4 Blade grid with intergrid hole boundary.

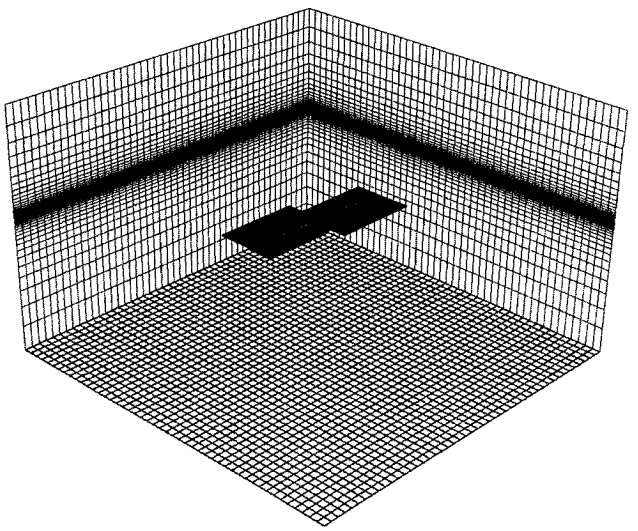

Fig. 5 Global background grid with blade system.

To improve interpolation, each blade grid lies within an intermediate grid. The intermediate grids are Cartesian with points concentrated at the blade's vicinity as shown in Fig. 4. The grids extend from the hub rotation axis to approximately five blade chords from the upper surface, seven chords from the lower, four chords in front, seven chords behind, and five chords from the tip. Each grid contains 75 points spanwise, 75 points chord, and 41 points from bottom to top. Figure 4 illustrates boundary planes within an intermediate grid with the blade grid cutting through it.

The global background grid shown in Fig. 5 completes the overset grid system. The global grid extends to four blade radii from the hub center upstream, downstream, and to the sides. The grid also extends two blade radii above the blade and two and one-half radii below. The grid consists of a total of 95 × 95 × 51 points with points clustered vertically in the rotor disk vicinity.

The entire moving overset system totals 1.62 million grid points. During the grid motions, the background grid remains stationary as the blade and intermediate grids rotate together through it. Figure 5 highlights the relative positions of the intermediate and blade grids with respect to the background grid. The intermediate grids move only in rotation about the spin axis and subsequently create hole regions within the background grid. The blade grids also rotate about the spin axis, but then also pitch and flap about those respective axes. During their pitch and flap motions the blade grids create holes within the intermediate grid as shown in Figs. 3 and 4.

Flight Test Conditions

The flight conditions chosen as a validation case comes from the flight tests documented by Cross and Watts[20] and Cross and Tu.[21] This test was chosen because of its extensive load survey, acoustic measurements, and detailed blade harmonics data. In addition, select flight conditions have been computed by two other numerical methods.[9,10] Both methods showed good correlations with the flight test data.

The flight tests were performed with the AH-1G helicopter at NASA Ames Research Center. The rotor is a two-bladed rectangular-planform teetering rotor with the operational loads survey (OLS) symmetrical airfoil section, and a linear twist of −10 deg from root to tip. Each blade has an AR of 9.8.

The forward-flight case chosen is test point no. 2157 reported in Cross and Watts.[20] This flight condition has an advance ratio of 0.19, hover tip Mach number of 0.65, flight Reynolds number of 9.73×10^8, and a rotor thrust coefficient equal to 0.00464. These conditions correspond to a forward speed of 82 kn at a rotor rotation rate of 315.9 rpm.

The first blade harmonics reported by the flight test were used to prescribe the rotor blade motions. Table 1 lists the blade harmonics.

Results and Discussion

The results were computed on the Numerical Aerodynamic Simulation Facility's Cray C-90 computer located at NASA Ames Research Center. The time-accurate calculation impulsively starts from freestream conditions with the viscous no-slip boundary condition applied at the blade surfaces. The time steps for this rotor blade system correspond to approximately 0.3125 deg of rotation or a nondimensional time step of 0.082. Each rotor revolution requires about 1152 time steps. The complete unsteady computation required a total of 45 h of single processor CPU time for five complete rotor revolutions producing approximately 40 Gbytes of flowfield data.

As noted in the previous section, the computed results used the first blade harmonics as measured by the flight test. However, the blade collective was corrected to the value recommended by Ramachandran et al.,[10] which allowed them to match the measured value of thrust. No further trim of the rotor was attempted in the present investigation with the result that the computed thrust was about 1.8% too low. In addition, the rotor was approximately balanced in rolling (lateral) hub

Table 1 Blade first harmonics, test point 2157

θ_0, deg	θ_{1s}, deg	θ_{1c}, deg	β_{1s}, deg	β_{1c}, deg
6.0	−5.5	1.7	−0.15	2.13

$\mu = 0.19$, $M_T = 0.65$, $Re = 9.73 \times 10^6$, and $C_T = 0.00464$.

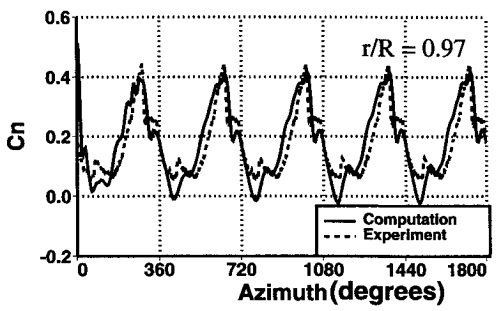

Fig. 6 Time history of normal force coefficient.

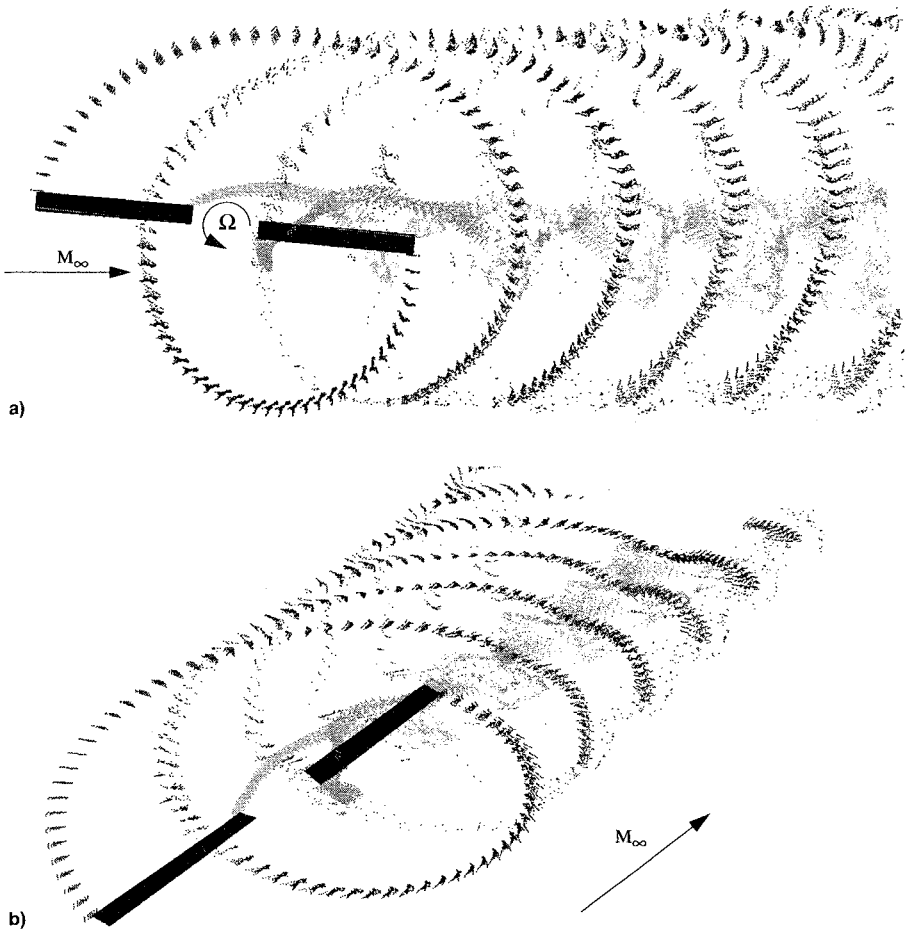

Fig. 7 Computed flow visualization using unsteady streak-line particles. Particles are released at inboard and outboard blade tip every 5 deg of azimuthal rotation. Traces shown for total five rotor revolutions. Flow periodicity is approximately established after second revolution: a) top view and b) perspective view.

moment and out of balance in pitching (longitudinal) hub moment. The important point is that the overall method is stable, it predicts airloads that agree well with the flight test, and it lays the foundation for more complete trim computations by including an appropriate dynamic model.

Figure 6 shows one of the blade's normal force coefficient time history at $r/R = 0.97$. The solid line is the computation, whereas the dashed line is the experiment. The figure shows that the normal force has an initial transient that exists for the first rotor revolutions and then becomes periodic.

Figures 7a and 7b illustrate unsteady particle streak-line patterns after five rotor revolutions. The unsteady flowfield analysis tool (UFAT) by Lane[22] at NASA Ames Research Center computed these unsteady streak lines. Rakes of particles were released every 5 deg of rotation along a plane of points just behind each blade's tip and root trailing edge. Each rake has a different shading to distinguish them from each other.

Figure 7a illustrates a top view of the highly complex flowfield caused by the wakes interacting with the blades. The particles released from a leading-blade cross over the following blade, showing evidence of blade vortex interaction. The particles also show evidence of excessive wake diffusion. Ideally, the tip vortices should maintain their core radius and intensity. The computed streakline particles remain close to each other initially, but when they encounter the following blade they tend to diffuse. This behavior indicates that the overset grid interpolations may be affecting the solution.

With the present grids, once the wake leaves the blade it must pass through five intergrid boundaries (blade grid to intermediate grid to background grid back to intermediate and then another intermediate to blade). The interpolation process tends to degrade the solution because of the required interpolation at the boundaries and the disparate grid resolutions. The number of intergrid boundary interpolations can be reduced by either changing the intermediate grid positions or consolidating the two separate intermediate grids into one with more effectively distributed points.

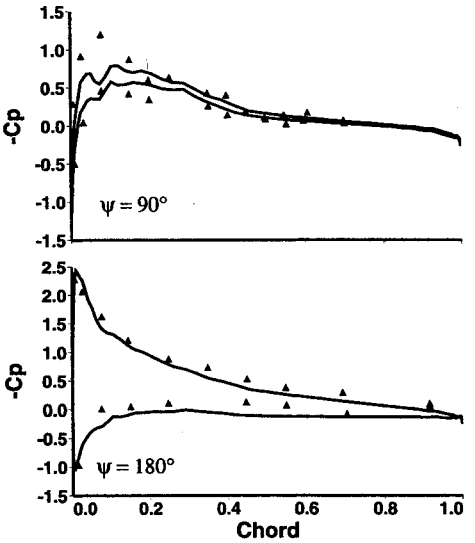

Fig. 8 Surface pressure coefficient $r/R = 0.60$; ▲, flight; ——, computation.

The streak-line patterns in Fig. 7 also demonstrate the rotor wake descent and roll-up. The particles released from the

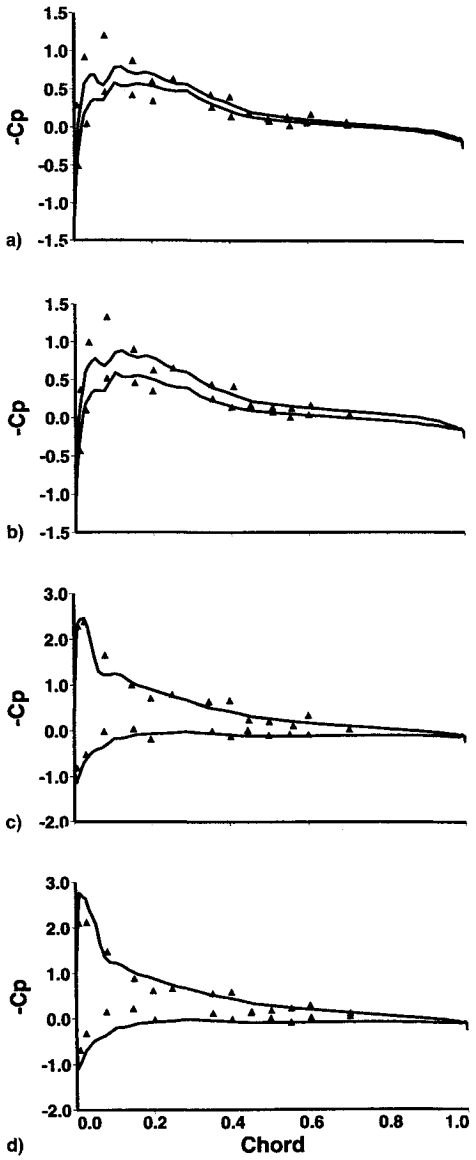

Fig. 9 Computed and measured blade surface pressure coefficient distributions, r/R = 0.97; ▲, flight; ——, computation. ψ = a) 90, b) 105, c) 270, and d) 300 deg.

blade roots descend further than those from the tips. This behavior illustrates the wake roll-up process. It also gives more insight into the wake diffusion as the particles continue to spread in the far-field background grid. This region has no intergrid boundary points; therefore, the wake diffusion is inherent to the solution and can only be controlled by adequate grid resolution.

The fuselage, hub, and other control surfaces have a significant effect on the blade loads. Although this simulation neglects those important components, the overall load and surface pressure comparisons have fair agreement with the flight test. The following load comparisons give considerable confidence in the computations.

Calculated and measured pressure coefficients are presented in Figs. 8 and 9 for different azimuthal and radial locations. Figure 8 shows the pressure distribution at the inboard radial station 0.6. The solid line is the computed solution while the symbols represent the experimental value. Note that the scales are different for each pressure plot. Towards the upper surface leading edge, the inboard stations' pressure distributions either overshoot or underpredict the pressure, while the ψ = 180-deg position compares fairly well with a difference in the trailing-edge pressures.

Figure 9 gives the surface pressure distributions at a radial station of r/R = 0.97. Again, the solid line is the computed solution while the symbols represent flight data. The lower surface pressures are well predicted for both advancing and retreating sides, except at 300 deg. The upper surface advancing and retreating sides have a consistent trend. For the advancing blade, the upper surface consistently underpredicts the leading-edge pressure towards the leading edge. On the retreating side, the upper surface pressures compare well with the experiment with some small overshoots. Hernandez and Johnson[9] found similar behavior in their predicted pressure distributions.

At all radial stations, the calculated pressure distributions depict irregular behavior towards the leading-edge region; especially at 90 deg in Figs. 8 and 9. A preliminary analysis of the airfoil coordinates of the associated surface slopes and inviscid two-dimensional airfoil calculations suggests that errors in the input blade geometry's leading-edge region causes these irregularities. The same effects appear in the results of Hernandez and Johnson,[9] who used the same input data. This discrepancy needs to be corrected in future work.

Figure 10 compares the unsteady measured (dashed line) and calculated (solid line) airloads of the fifth computed rotor

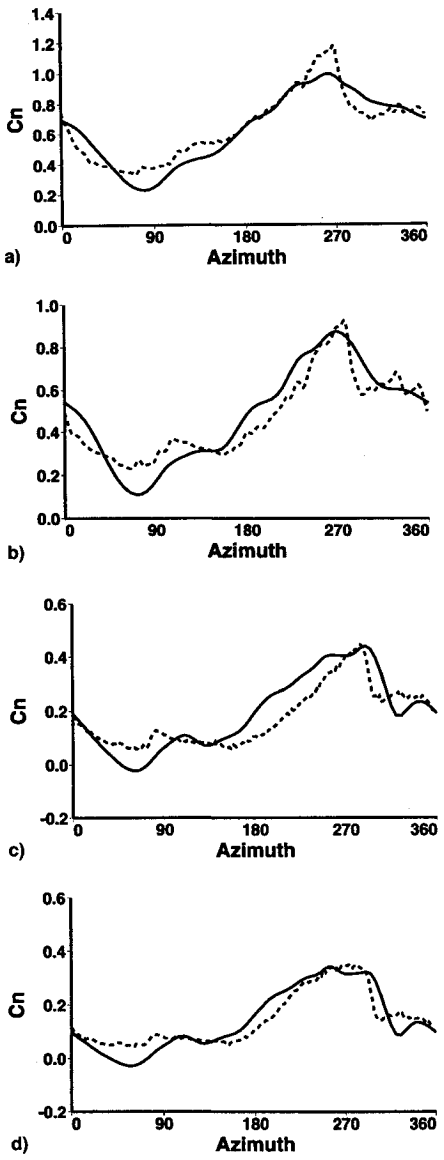

Fig. 10 Computed and measured blade normal force coefficients showing the blade-vortex interaction; ---, flight; ——, computation. r/R = a) 0.60, b) 0.75, c) 0.97, and d) 0.99.

Table 2 Computed and flight test rotor force and moment coefficients

	C_T, thrust	C_Q, torque	C_{Mx}, longitudinal	C_{My}, lateral
Computed	0.00455	0.000227	−0.00022	0.000008
Flight	0.00464	0.0002196	0.0	0.0

$\mu = 0.19$, $M_T = 0.65$, $Re = 9.73 \times 10^6$, and $\sigma = 0.0651$.

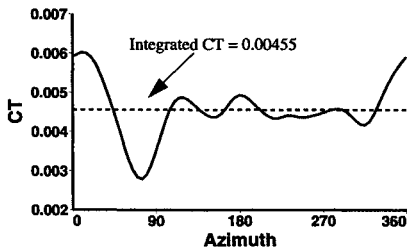

Fig. 11 Time history of rotor thrust.

revolution at various radial locations. The figures show strong blade vortex interaction for the advancing blade around azimuthal locations of 70–90 deg and on the retreating side around 270 deg. The loads are underpredicted for the advancing side. At the retreating side, loads are slightly underpredicted for the cases presented here. Blade-vortex interactions at outboard stations seem stronger as indicated by the negative lift.

Table 2 lists the computed rotor force and moment coefficients. As shown, the rotor is not trimmed in pitch, but essentially trimmed in roll. The power is overpredicted by approximately 15%.

Figure 11 illustrates the time variation of the integrated rotor thrust for the fifth rotor revolution. The solid line presents the predicted azimuthal variation while the dashed line represents the time averaged or gross rotor thrust. The gross thrust agrees within 1.8% of the gross weight of the aircraft in flight.

Conclusions and Future Work

The unsteady forward-flight flowfield of the AH-1G helicopter's two-bladed rotor system was computed by solving the thin-layer Navier–Stokes equations on moving overset grids. The resulting flowfield visualizations and airload comparisons verify the method's versatility for rotorcraft problems. The method efficiently obtained periodic solutions within three rotor revolutions. Unsteady streak lines showed the significant blade vortex interactions and wake roll-up. In addition, the streak-line patterns showed that grid resolution needs improvement in the rotor wake to reduce diffusion in the wake. Blade surface pressures compared well with the flight test data, especially at the retreating side. This comparison was somehow surprisingly better in the inboard section. Leading-edge surface pressure irregularities point to errors in the original airfoil coordinate definitions. The spanwise and integrated load data also correlates fairly well with the flight airload data and previous computations.

Although the rotor was only partially trimmed, these results demonstrate the method's capabilities. To trim the rotor properly, one would need to include blade dynamics by tightly coupling the unsteady load prediction to a suitable dynamics model, which is a straightforward extension to the present formulation. This coupling would also allow for aeroelastic effects such as torsion and bending. The inclusion of a fuselage through additional overset grids would further improve the solutions.

Acknowledgments

The authors would like to thank K. Ramachandran for providing the blade surface geometry and all of his subsequent help in this work. We would also like to thank Jeffry L. Cross for providing valuable information regarding the flight test. Finally, the authors wish to express their appreciation to W. J. McCroskey for his help and encouragement.

References

[1]Duque, E. P. N., and Srinivasan, G. R., "Numerical Simulation of a Hovering Rotor Using Embedded Grids," *Proceedings of the 48th AHS Annual Forum and Technology Display* (Washington, DC), American Helicopter Society, 1992.

[2]Srinivasan, G. R., Baeder, J. D., Obayashi, S., and McCroskey, W. J., "Flowfield of a Lifting Rotor in Hover: Navier-Stokes Simulation," *AIAA Journal*, Vol. 30, No. 10, 1992, pp. 2371–2378.

[3]Srinivasan, G. R., and Baeder, J. D., "TURNS: A Free-Wake Euler/Navier-Stokes Numerical Method for Helicopter Rotors," *AIAA Journal*, Vol. 31, No. 5, 1993, pp. 959–962.

[4]Chen, C. L., and McCroskey, W. J., "Numerical Solutions of Forward Flight Rotor Flow Using an Upwind Method," AIAA Paper 89-1846, June 1989.

[5]Agarwal, R. K., and Deese, J. E., "A Euler Solver for Calculating the Flowfield of a Helicopter Rotor in Hover and Forward Flight," AIAA Paper 87-1427, June 1987.

[6]Johnson, W., *CAMRAD/JA; A Comprehensive Analytical Model of Rotorcraft Aerodynamics and Dynamics*, Vol. I, Johnson Aeronautics, Palo Alto, CA, 1988.

[7]Strawn, R., and Tung, C., "The Prediction of Transonic Loading on Advancing Helicopter Rotors," NASA TM-88238, United States Army Aviation Systems Command, USAVSCOM TM 86-A-1, April 1986.

[8]Strawn, R., Desopper, A., Miller, J., and Jones, A., "Correlation of PUMA Airloads-Evaluation of CFD Prediction Methods," Fifteenth European Rotorcraft Forum, Amsterdam, Sept. 1989.

[9]Hernandez, F., and Johnson, W., "Correlation of Airloads on a Two-Bladed Helicopter Rotor," International Specialist Meeting on Rotorcraft Acoustics and Rotor Fluid Dynamics, PA, Oct. 1991.

[10]Ramachandran, K., Schlechtriem, S., Caradonna, F. X., and Steinhoff, J. S., "Free-Wake Computation of Helicopter Rotor Flowfield in Forward Flight," AIAA Paper 93-3079, July 1993.

[11]Steger, J. L., Dougherty, F. C., and Benek, J. A., "A Chimera Grid Scheme," *Advances in Grid Generation*, edited by K. N. Ghia and U. Chia, American Society of Mechanical Engineers FED-5, 1983, pp. 59–69.

[12]Meakin, R., "Moving Body Overset Grid Methods for Complete Aircraft Tiltrotor Simulations," AIAA Paper 93-3350, July 1993.

[13]Srinivasan, G. R., and Ahmad, J. U., "Navier-Stokes Simulation of Rotor-Body Flowfield in Hover Using Overset Grids," Nineteenth European Forum, Cernobbio, (Como) Italy, 1993.

[14]Yoon, S., and Jameson, A., "An LU-SSOR Scheme for the Euler and Navier-Stokes Equations," AIAA Paper 87-0600, Jan. 1987.

[15]Van Leer, B., Thomas, J. L., Roe, P. L., and Newsome, R. W., "A Comparison of Numerical Flux Formulas for the Euler and Navier-Stokes Equations," AIAA Paper 87-1104, June 1987.

[16]Baldwin, B. S., and Lomax, H., "Thin-Layer Approximation and Algebraic Model for Separated Turbulent Flow," AIAA Paper 78-0257, Jan. 1978.

[17]Johnson, W., *Helicopter Theory*, Princeton Univ. Press, Princeton, NJ, 1980.

[18]Amirouche, F. M. L., *Computational Methods in Multibody Dynamics*, Prentice-Hall, Englewood Cliffs, NJ, 1992.

[19]Chan, W. M., Chiu, I. T., and Buning, P. G., "User's Manual for the Hyperbolic Grid Generator and the HGUI Graphical User Interface," NASA TM 108791, Oct. 1993.

[20]Cross, J. F., and Watts, M. E., "Tip Aerodynamics and Acoustics Test," NASA Ref. Pub. 1179, Dec. 1988.

[21]Cross, J. F., and Tu, W., "Tabulation of Data from the Tip Aerodynamics and Acoustics Test," NASA TM 102280, Nov. 1990.

[22]Lane, D. A., "UFAT—A Particle Tracer for Time-Dependent Flow Fields," *Proceedings of IEEE Visualization '94* (Washington, DC), 1994, pp. 257–264.